



ELSEVIER

Optics and Lasers in Engineering 39 (2003) 345–368

OPTICS and LASERS
in
ENGINEERING

Nanostructured silicon as a photonic material

L. Pavesi*, Z. Gaburro, L. Dal Negro, P. Bettotti,
G. Vijaya Prakash, M. Cazzanelli, C.J. Oton

INFN and Dipartimento di Fisica, Università di Trento, via Sommarive 14, 38050 Povo, Italy

Received 31 July 2001; accepted 17 August 2001

Abstract

Photonics applications of silicon are presented. In particular it is demonstrated that silicon when rendered low dimensional, e.g. in form of nanocrystals or quantum wires, can be turned into an active photonic materials which shows light amplification characteristics, non-linear optical effects, photon confinement in both one and two dimensions, photon trapping with evidences of light localization, and gas sensing properties.

© 2002 Elsevier Science Ltd. All rights reserved.

Keywords: Silicon; Silicon nanocrystals; Photonics; Gain in silicon; Microcavities; Photonic band-gap crystals; Light localization; Interferometry; Non-linear optical effects; Gas sensors

1. Introduction

Silicon at the beginning of the second millennium is experiencing a new phase as a functional material. In fact, after ten years of intense research many expectations exist that it can enter the field of photonics with a leading role [1] and not only as a passive or substrate material. Indeed the observation by our group in collaboration with the team led by Priolo of optical gain in nanostructured silicon [2] has broken the barrier to a silicon laser and many research efforts are now spent towards this goal.

One can cause the reason of our interest in the field, when many other materials are outperforming silicon with this respect. However, the microelectronics revolution of last century is mainly based on the availability of a single material and a single technology which dominates the industry, that of silicon. Investors are thinking that

*Corresponding author. Tel.: +39-046-1881605; fax: +39-0461-881696.

E-mail address: pavesi@science.unitn.it (L. Pavesi).

the lack of a similar scheme for photonics will prevent a real diffusion of this technology in every day life. We propose silicon as the key material or the unifying materials in order to develop common frame in which integrate the various material for specific applications.

In this paper we will review our activity in the field by presenting many different research topics on which we are currently engaged. We firstly review our results on gain in silicon nanocrystals, then we present some recent measurements on the non-linear optical properties of silicon nanocrystals measured by the *z*-scan techniques. Section 4 reports on a technique to grow optical microcavities within a silicon foundry, that is via a CMOS-compatible process. If in Sections 2–4 we were concerned on low dimensional silicon where the electronic properties of the material were changed in view of an increased recombination efficiency, in Section 5 we present how introducing photon confinement it is also possible to modify the optical properties of silicon. This we realize through the building of photonic band-gap crystals. In Section 5 we report on the way to produce them and the way to measure their optical properties. Section 6 reports on an interferometry technique to monitor the parameters of porous silicon during the etch. This allows the growth of extremely high quality multilayers. Section 7 concerns the measure of the light localization properties in deterministic disordered one-dimensional photonic crystals based on porous silicon multilayers. We report on the slowing down of the photon diffusion and beating of photon modes. Section 8 is more applied in content and it is about the exploitation of low dimensional silicon as the sensing material in optoelectronic gas sensor.

As a general introduction to the field we refer the reader to the book [3] or to the review paper [4]. Clearly many of the results presented here have been taken within collaboration with other groups and are detailed lengthly in the original publications to which we refer the reader too.

2. Optical gain in silicon

For a laser, one needs three things: an active material, an optical cavity and an efficient pumping scheme. Up to now, silicon was considered as a prohibitive material for a laser, as it was assumed it was physically inadequate to amplify light. However, when silicon is shaped into nanocrystals its physical properties dramatically change. Quantum confinement effects coupled with localization of carriers in defect free regions, allow efficient room temperature emission from silicon nanocrystals. Here we report on an investigation of silicon nanocrystals to demonstrate that they can amplify light, i.e. the first requirements for a silicon laser can be fulfilled by silicon nanocrystals.¹

Low dimensional silicon nanocrystals (NS) have been produced by ion implantation ($80 \text{ keV} - 1 \times 10^{17} \text{ Si/cm}^2$) into ultra-pure quartz substrates or into

¹This work has been performed in collaboration with the group of Prof. Priolo of INFN and University of Catania and the group of Dr. Iacona at IMETEM-CNR. It has been carried out in the frame-work of the special project LUNA and the advanced research project RAMSES of INFN.

thermally grown silicon dioxide layers on Si substrates, followed by high temperature thermal annealing (1100°C—1 h). Transmission electron microscopy of these samples showed the presence of NS embedded within the oxide matrix. They were formed in a region centred at a depth of 110 nm from the sample surface and extending for a thickness of 100 nm; they were ~ 3 nm in diameter and with a concentration of $\sim 2 \times 10^{19} \text{ cm}^{-3}$. Considering the different effective refractive indices of the NS containing region and of quartz, this sample structure identifies a waveguide.

Luminescence spectra under low excitation power at room temperature are shown in Fig. 1. A single wide emission band peaked at 800 nm, characteristic of the radiative recombination of carriers in NS, is observed. The luminescence is attributed to a Si=O interface state, formed at the interface between the Si nanocrystals and the SiO₂ matrix [5].

To measure light amplification we used the variable stripe length (VSL) method (see Fig. 2) [6]. The sample is optically excited by an UV extended Ar laser ($\lambda = 360$ nm) in a stripe-like geometry with variable length (ℓ). The amplified spontaneous emission intensity I_{ASE} emitted from the sample edge is measured as a function of ℓ . Even though the experimental method used is very standard, particular care has to be applied in order to avoid spurious effects [2]. The variable stripe length method is thus based on the measure of the luminescence exiting from the sample edge as a function of the extent of the excited region. From a fit of the resulting curve, the optical gain g can be deduced at every wavelength. By assuming a one-dimensional amplifier model, I_{ASE} can be related to g by [6]:

$$I_{\text{ASE}}(\ell) \propto \frac{I_{\text{SPONT}}}{g - \alpha} (e^{(g-\alpha)\ell} - 1), \quad (1)$$

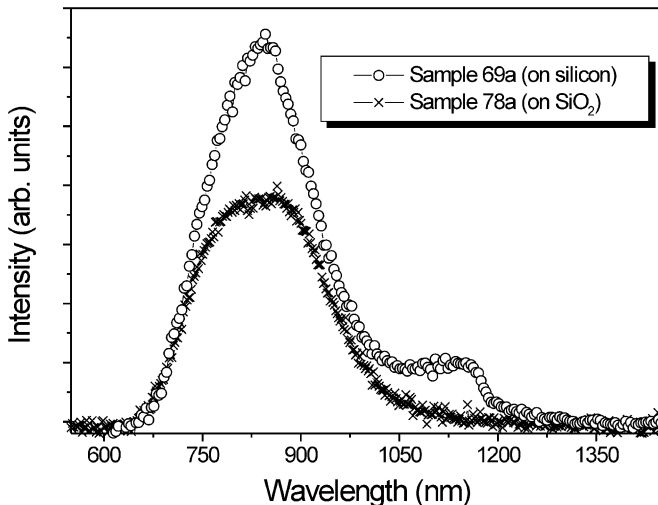


Fig. 1. Room temperature luminescence of Si nanocrystals embedded in a quartz matrix (sample 78a) or in thermal oxide (sample 69a). The 488 nm line of an Ar laser excited the luminescence.

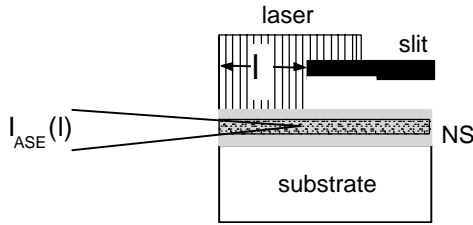


Fig. 2. Sketch of the variable stripe length method. The amplified luminescence intensity from the sample edge is recorded as a function of the slit width ℓ .

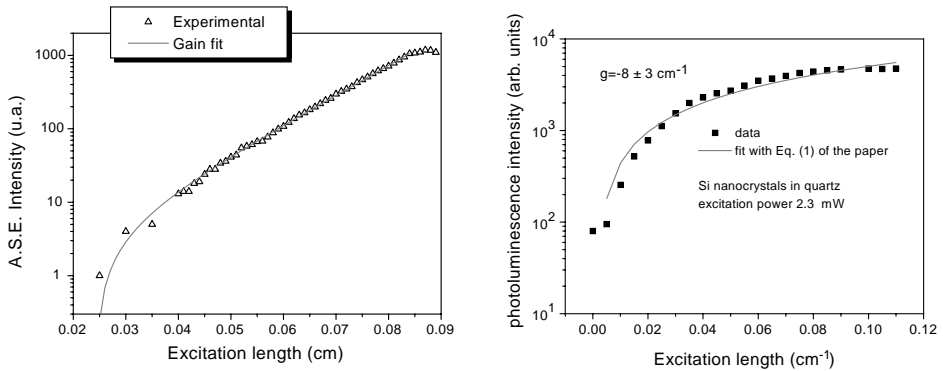


Fig. 3. (left) Photoluminescence intensity as a function of the excitation length (i.e. slit width) for an excitation power of $J_{\text{exc}} = 1.5 \text{ kW/cm}^2$. The fit of the experimental data points with the gain equation yields a value for the net modal gain of $g = 100 \text{ cm}^{-1}$. (right) Photoluminescence intensity as a function of the excitation length (i.e. slit width) for an excitation power of $J_{\text{exc}} = 7 \text{ Wcm}^{-2}$. The fit of the experimental data points with the gain equation yields a value for the net modal gain of $g = -8 \text{ cm}^{-1}$, i. e. absorption.

where I_{SPONT} is the spontaneous emission intensity and α an overall loss coefficient. The gain measured in this way is the modal gain [7]. Fig. 3 shows I_{ASE} vs. ℓ in Si NS measured at a wavelength of 800 nm. When an excitation power in excess of 1 kW cm^{-2} is used (Fig. 3 left), an exponential increase of the amplified spontaneous emission is observed as ℓ increases. On a region of $500 \mu\text{m}$ I_{ASE} increases of more than three orders of magnitude. On the contrary, when the excitation power is low (Fig. 3 right), I_{ASE} slightly increases for $0 < \ell < 1000 \mu\text{m}$. This behaviour is typical of an absorbed beam. A fit of these data with Eq. (1) yields a net modal gain $g - \alpha = 100 \pm 10 \text{ cm}^{-1}$ for the data on the left and $g - \alpha = -8 \pm 3 \text{ cm}^{-1}$ for the data on the right, i.e. absorption at low pump powers and gain at high pump power. The same overall behaviour was observed for NS formed on silicon wafer or on quartz.

The spectral shape of the gain data can be determined in a region where I_{ASE} is exponentially increasing. In Fig. 4, we show the spectral dependence of the gain. It is flat in the region around 750 nm, while for longer and shorter wavelengths negative gain values are observed.

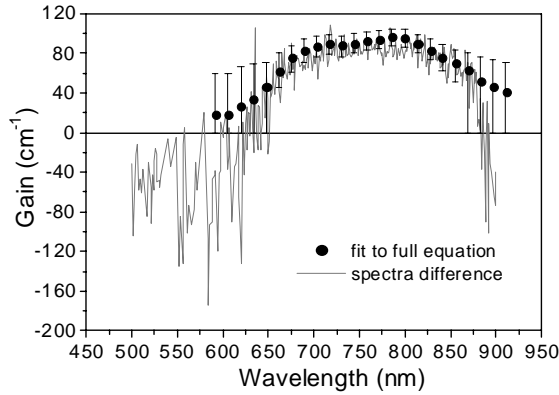


Fig. 4. Spectral dependence of the gain.

Table 1
Gain cross section per quantum dot/nanocrystal determined for various material systems

Quantum dot material	Net modal gain (cm ⁻¹)	Net material gain (× 10 ⁴ cm ⁻¹)	Areal dot density (cm ⁻²)	Active layer thickness (nm)	Filling factor (× 10 ⁻⁴)	Gain cross section per dot (× 10 ⁻¹⁶ cm ²)
InAs Single QD layer [9]	8.2	9 ^a	1 × 10 ¹¹	1.7	1.2	1200
InAs 7 QD stacks [10]	70–85	1.5 ^a	1 × 10 ¹¹	100	48	4000
GaAs Single QD layer [8]	13 ^a		1 × 10 ¹⁰			450 ^a
Si NS	100	1	2 × 10 ¹⁴	100	970	0.5–5

^a Calculated approximately.

By using the calculation of Ref. [8], it is possible to extract from the measured gain g the gain cross section per single nanocrystal γ . In such a way a meaning full comparison among results from different techniques and among different materials can be performed. In Table 1 we compare the values we got for NS to the gain cross sections per quantum dot (QD) for some III–V semiconductors [8–10]. NS values are about three orders of magnitude lower than the one typically found in InAs quantum dots (QD) [9,10], due to the indirect band-gap of Si. Despite this difference, the net material gain is of the same order of magnitude between Si NS and InAs QD systems due to the much higher areal density of NS achievable with the ion-implantation method used in this work.

To build a model to understand the gain data, we consider two facts: (a) in the literature there exist some proofs that silicon and other silicon based systems do not show any optical gain for *interband* transitions due to the presence of a strong free carrier absorption which prevents the population inversion, (b) the 800 nm band is due to interface states related emission. Taking into account this, we propose a three levels model to explain the gain (Fig. 5), where gain is due to inversion of the radiative interface states caused by the Si-O double bond with respect to the NS

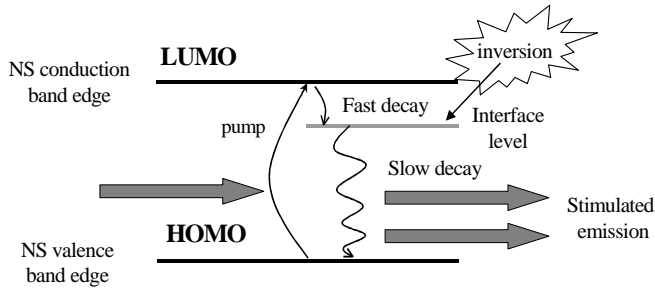


Fig. 5. Model of gain in silicon nanocrystals (NS). LUMO and HOMO stands for lowest unoccupied molecular orbital and Highest occupied molecular orbital.

ground state. Direct interband transitions between electron and holes or free excitons in the nanocrystals are ruled out due to: (a) the absence of previous observation of gain in Si based systems due to interband transitions, and (b) the weak energy dependence of the spectral position of the emission related to Si nanocrystals already reported in the literature. More detailed analysis of the data and the model reported here are presented in Ref. [2].

3. Non-linear optical properties of silicon nanostructures measured by z-scan

Besides the gain properties, Si NS are most promising materials for non-linear applications as well.² Many authors have studied the non-linear optical properties of Si NS by using porous silicon [11]. As porous silicon is a complicate material, we have taken up the study of the non-linear optical properties of a cleaner system, that is plasma enhanced chemical vapor deposition (PECVD) grown Si NS. Here we report some of the results of such studies: the sign and magnitude of both real and imaginary parts of third-order non-linear susceptibility $\chi^{(3)}$ measured by the z-scan method [12]. A single gaussian beam is focused in a tight geometry, as shown in Fig. 6. By measuring the transmission through a non-linear medium via a finite aperture in the far field as a function of sample position z with respect to the focal plane of the lens, it is possible to infer the non-linear susceptibility. In fact the power dependence of the refractive index of a material $n = n_0 + n_2 I$ causes the sample to act as a lens. By using an open aperture it is also possible to evaluate the non-linear absorption coefficient (β), where β is related to the linear absorption coefficient α_0 as $\alpha = \alpha_0 + \beta I$.

The Si NS are obtained by thermal treatments of substoichiometric SiO_x films, deposited by PECVD and prepared within the institute IMETEM-CNR by Iacona. 230 ± 30 nm thick substoichiometric films are deposited on a quartz substrate [13]. High temperature annealing of the films induces a phase separation between Si and

²This work has been supported by MURST through the program COFIN99 coordinated by S. Modesti.

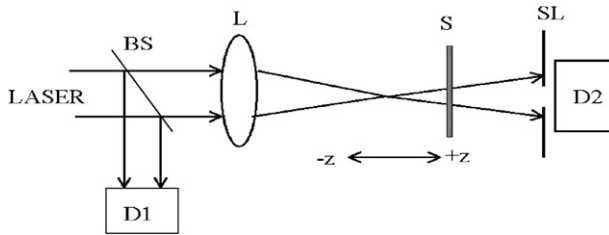


Fig. 6. A schematic representation of z -scan set up. D1, D2 are Si-detectors, BS = beam splitter, L = lens, S = sample and SL = a slit.

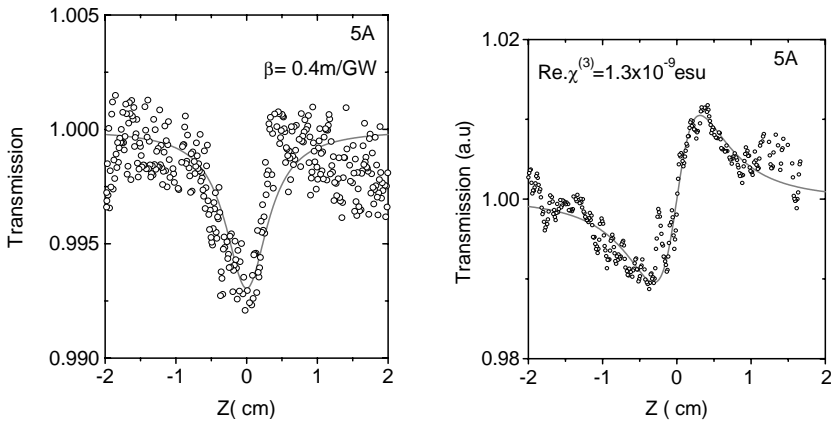


Fig. 7. (left) Open aperture z -scan data for sample 5A. Solid line is a theoretical fit at peak intensity 7.5 GW/cm^2 . (right) Closed aperture z -scan data for sample 5A. Solid line is a theoretical fit at peak intensity 3.9 GW/cm^2 .

SiO_2 and as a consequence, Si NS are formed. The NS size depends on the excess Si amount as well as on the annealing temperature. The z -scan experiments were performed by using a gaussian laser beam from a Ti:Sapphire laser (wavelength, $\lambda = 813 \text{ nm}$, repetition rate 82 MHz and pulse width 60 fs) in a tight focus limiting geometry.

Fig. 7 left shows the normalized open aperture transmission (full power into the detector) as a function of z . A transmission dip is observed. By using a standard fitting procedure, a value for β is obtained [12]. Closed aperture (finite aperture at the far filed) z -scan measurements are shown in Fig. 7 right. Also in this case, a numerical fit of the experimental data yields the non-linear refraction index coefficient n_2 . The signature of the closed aperture for all the samples we studied shows a distinct valley-peak configuration suggesting a positive non-linear effects (self focussing) [11,12,14]. Quantitatively, the real part of $\chi^{(3)}$ was found in the range of $1.3\text{--}2.7 \times 10^{-9} \text{ esu}$ and the imaginary part of $\chi^{(3)}$ in the range of

$0.3\text{--}2.1 \times 10^{-10}$ esu. $\text{Re}\chi^{(3)} \gg \text{Im}\chi^{(3)}$, that is $\text{Re}\chi^{(3)}$, which gives the change in the refractive index, is dominant.

The non-linear absorption in most of refractive materials arises from either direct multiphoton absorption or saturation of single photon absorption. The open aperture z -scan traces for our samples shows a well defined bell shaped minimum transmittance at the focus, suggesting two photon related non-linear absorption, where the pump laser energy lies in the range $E_g < 2h\nu < 2E_g$, where E_g is the absorption band gap of the NS. Estimate of the indirect band gap of this sample lies between 2.75 and 3.63 eV [15], while the pump energy is at 1.53 eV (813 nm). The measured β values are higher than those for crystalline silicon [14] and close to the one reported for porous silicon [11]. The absolute values for $\chi^{(3)}$ are of same orders of magnitude as those reported for porous silicon [16], glasses containing microcrystallites [17] and close to those expected theoretically for low dimensional Si materials ($\chi^{(3)} \sim 10^{-8}$ esu) [18]. Similar to the observations made by the PL measurements, the third-order non-linear susceptibility values shows systematic changes with respect to Si NS size variation, increasing by decreasing the NS sizes [19,20]. A detailed analysis of this study is reported elsewhere.

4. Silicon/silicon dioxide multilayers for optical microcavities

In this section we review a technique to grow high quality nanometer thick Si/SiO₂ optical microcavities via Low Pressure Chemical Vapour Deposition (LPCVD).³ The growth process is CMOS-compatible to allow the direct implementation of these devices in an industrial environment. Briefly, the process is based on cyclic deposition of 20 nm thick poly silicon layers, which are thinned down to some nm through repeated oxidation and HF etching treatments [21]. The deposited thin Si-layers (<3 nm) show photoluminescence (PL) at room temperature ranging from 1.9 to 1.1 eV [21,22]. Based on the temperature dependence of the PL and the saturation of PL as a function of excitation power, the PL in the range 1.9–1.1 eV is attributed to radiative recombination of excitons in the confined Si-layers, whereas PL at energies higher than 1.9 eV is assigned to oxygen related defects in SiO₂ [21].

A similar fabrication process based on repeated deposition and oxidation of poly Si can be used to fabricate Fabry-Perot type planar microcavities. Microcavities allow the modification of the spontaneous-emission of an optical active material [23]. In the case of weak electron–photon coupling a spatial redistribution of the spontaneous emission into the resonance mode of the microcavity occurs. Whereas porous silicon microcavities are intensively studied [24], microcavities with SiO₂/Si superlattices, as the optical active material, have not been studied, yet. Our aim here is to report the realisation of an optically active Si/SiO₂ microcavities with interesting and promising optical properties. Microcavities consisting of two Distributed Bragg

³This work has been performed in collaboration with the Microsystem Division of ITC-irst, Dr. P. Bellutti and G. Pucker and financed by EC via the ESPRIT program SMILE. The TEM photographs are a courtesy of C. Spinella.

Table 2

Description of samples studied: Bottom Distributed Bragg Reflectors (DBR) is the DBR between Si-substrate and SiO₂ spacer, whereas the top DBR is the one between the spacer and the air. The superlattice is formed by 3 repetitions of 2 nm thick Si and 5 nm thick SiO₂ barrier layer^a

Sample	Bottom DBR a/b	Cavity	Top DBR a/b	Comment
B1	3/750	270 nm SiO ₂ followed by the superlattice	—	Half active cavity
B2	3/750	270 nm SiO ₂	—	The same as B1 without the superlattice
B3	3/750	Superlattice in center of SiO ₂ spacer of 600 nm	2/750	Active λ -microcavity
A1	2/690	425 nm SiO ₂	2/690	Passive λ -microcavity
C	—	Superlattice	—	Reference superlattice sample

^a Note: a refers to the number of periods of Si/SiO₂ $\lambda/4$ layers in the DBR. b refers to the centre of the stop band of the DBRs in nm.

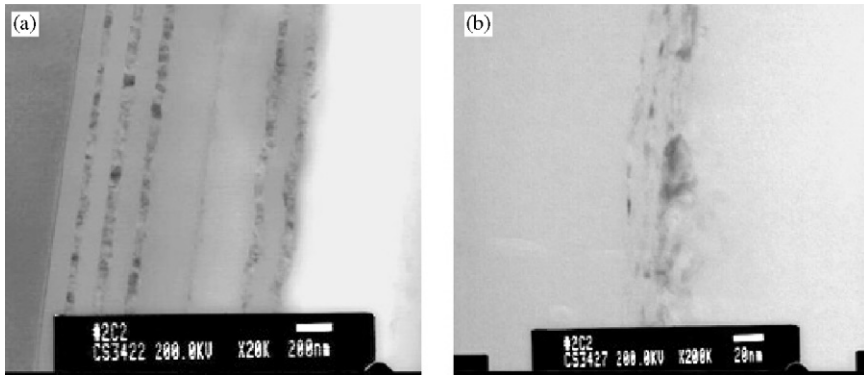


Fig. 8. (left) SEM images of the microcavity sample B3. The darker regions correspond to the Si layers. A magnified image of the central region of the microcavity is shown on the right. The region where the nanometric multilayers are formed is shown.

Reflectors (DBR, periodic repetition of $\lambda/4$ thick Si or SiO₂ layers) separated by a SiO₂ λ -thick spacer layer, where λ is the central cavity wavelength, were realized on p-type doped Si wafers. To obtain active microcavities, a nanometer thick SiO₂/Si superlattice was deposited in the middle of the spacer SiO₂ layer. The different samples studied are described in Table 2.

Fig. 8 shows the TEM images of the microcavity B3. The microcavity structure is clearly observed. In the centre of the SiO₂ spacer, a thin grey line reveals the presence of the nanometer thick SiO₂/Si superlattice. A blow-up of this region is reported in Fig. 8b. The superlattice is formed by three Si layers which are only partly seen as dark lines. Fig. 9 shows the reflectance spectra of the microcavity B3 together with

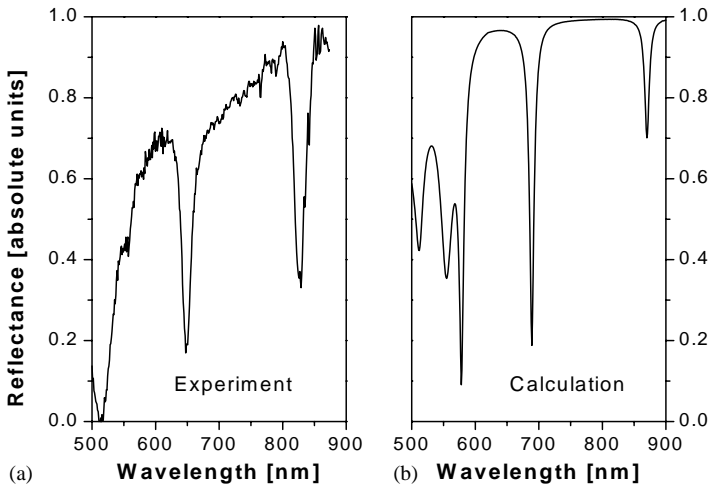


Fig. 9. Measured (Fig. 9a) and calculated reflectance spectra (Fig. 9b) of sample B3. A wavelength dependent refractive index and the thickness values obtained by SEM have been used in the calculations.

the computed spectra. Sample B3 shows a cavity resonance at 830 nm ($\Delta\lambda = 13$ nm, $Q = 65$). This cavity resonance position is the weighted average of the value due to the spacer ($\lambda_c = n_c L_c = 885$ nm where n_c and L_c are the refractive index and the thickness of the spacer, respectively) and the value centre of the stop band centre due to the DBR (estimated to be 750 nm) [25]. Beside the 830 nm cavity mode, a second resonance is observed at 650 nm. For an ideal planar microcavity (constant reflectivity), this second resonance is expected to be at $\frac{2}{3} \cdot \lambda_c = 590$ nm. The discrepancy is explained by the following reasons: (1) the DBRs are centred at 750 nm thus shifting the cavity mode to larger wavelengths; (2) both the imaginary and the real parts of the refractive index of Si are significantly increasing below 650 nm, thus resulting in an further shift to larger wavelengths. The calculation reported in Fig. 9b, where these effects are considered, gives the two cavity modes at 870 and 689 nm, values which are in reasonable agreement with the experimental ones. The observed difference in the lineshape between calculated and experimental spectra is probably due to scattering effects (roughness of the SiO₂/Si interfaces), which were not included in the calculation.

Fig. 10 shows the PL of the samples B1, B3 and C. Samples A1 and B2 showed no appreciable luminescence. The reference C sample shows a broad emission band peaked at 870 nm (1.4 eV) due to quantum confined excitons [21]. A similar emission feature is observed for the half-cavity B1 sample, but it is considerable stronger. The 20-fold luminescence enhancement can be related to two different contributions (1) the high-reflecting mirror, reflecting both the exciting laser and the emitted light explains a luminescent enhancement by factor of ≈ 4 , (2) the larger roughness of the superlattice layers (see Fig. 8b), with respect to the roughness of the superlattice of

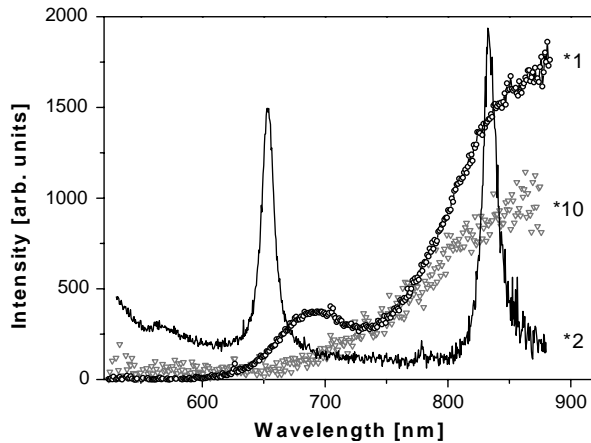


Fig. 10. Room temperature photoluminescence spectra of the half-cavity B1 sample (triangles), the microcavity B3 sample (straight line) and the reference superlattice C sample (circles). The excitation wavelength was 488 nm. Spectra of the B3 sample and the C sample have been multiplied by 2 and 10, respectively.

sample C [21]. The enhanced luminescence of Si nanostructures with increasing roughness can be explained by an increase in the quantum confinement [26].

The photoluminescence of sample B3 shows the two cavity modes at 830 and 650 nm, respectively, and weak emissions at higher energies due to the leaky cavity modes. The intensity of the 830 nm emission equals the one of the half cavity B1 sample in the same spectral region. However, excitation of the superlattice is less effective for sample B3, since the exciting laser light is partly reflected and absorbed by the top DBR. Additionally, the sample B3 shows intense emission at the 650 nm resonance and at even higher energies, due to oxygen related defects, which are induced by the presence of the SiO₂/Si superlattice. Microcavities without a superlattice inside the spacer do not show any PL. Why the high energy emission in sample B3 is significantly larger than in sample B1 is not entirely clear. It may be possible that the exciton–photon coupling in the microcavity modifies the ratio between non-radiative and radiative recombination at 650 nm. Instead of relaxing to low energy states, excitons couple with the resonance optical mode at 650 nm and recombine radiatively.

5. Macroporous silicon as a template to photonic band-gap crystals

A general introduction to photonic band-gap crystals can be found in [27].⁴ Our group activities on this topics is devoted to the synthesis of photonic structures,

⁴This work has been made possible by collaboration with the groups of Prof. Andreani and Prof. Marabelli of INFN and University of Pavia and sponsored by MURST through the program COFIN00 coordinated by L.C. Andreani

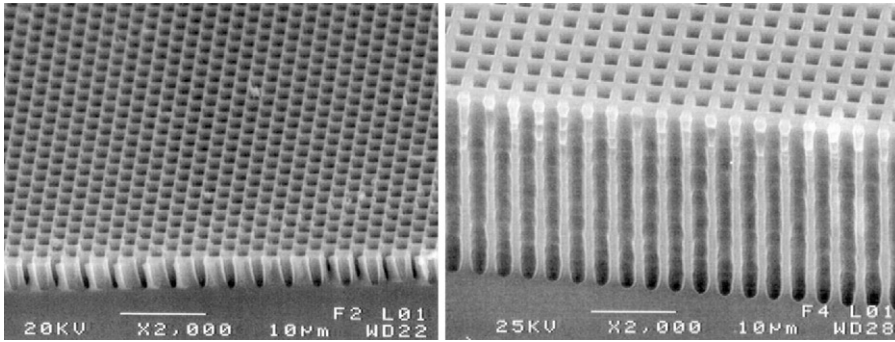


Fig. 11. Representative SEM images of two photonic crystals formed by macroporous silicon samples obtained on n-type silicon (8–12 Ωcm), but with different lattice symmetries.

made in silicon and produced by electrochemical etching. We exploit the possibility of anisotropically etch the semiconductor, when it is immersed in an HF solution and biased anodically [4]. The obtained structures are formed by a regular array of pores in a silicon matrix (Fig. 11). The optical properties of these lattices are well described by a formalism very similar to the one used in solid state physics for describing the electron dispersion law: the periodic dielectric lattice (pores in silicon) produces a modified dispersion law for photons, with the formation of photonic bands, separated by range of frequencies in which the propagation of the radiation inside the matter is forbidden, photonics gap.

The synthesis via electrochemical etching is a process fully compatible with the CMOS technology and easily portable in a microelectronics environment. To obtain pores, the samples are immersed in a solution of HF, contained in a Teflon cell. The acid is diluted in water and ethanol, the latter needed to increase the wettability of silicon. During the etch the substrate is biased positively. The exact mechanism of dissolution of silicon is not yet well understood [28,29]. What we know is that holes are needed near the interface of the silicon-electrolyte junction to etch the silicon. The carriers can interact with the oxidant (F^-) to break the silicon bonds and promote the dissolution. The anisotropy of the etching is due to the different etching rates that are developing on the tips and on the walls of the pores. At the tips, the highest curvature radius is responsible for an highest electric field, where the carriers are preferentially collected. It is implicit that above a critical carrier density, the tips of the pores are no longer able to consume all the holes, dissolution then starts to occur also on the pore walls. In this regime we have the electropolishing of the semiconductor. As for the details, it is necessary to distinguish between p- and n-type doped silicon (Fig. 12) [30,31]. In n-type doped substrates, holes have to be photogenerated by illuminating the back of the substrate. Due to the applied bias, they diffuse to the surface where they enter the solution at the pore tips. The limiting process is the hole diffusion. In the case of p-type silicon, holes are always present, and

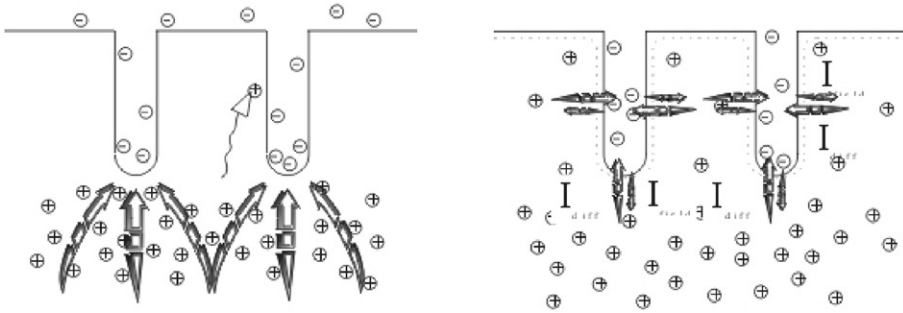


Fig. 12. On the left is sketched the dissolution mechanism for n-type silicon, in which the semiconductor between two adjacent pores is totally depleted of carriers. On the right is show how the dissolution works for p-type silicon, with the lateral currents responsible of the widening of the pores during etching.

is sufficient to induce a current during the etching to produce macro-pores. These two different mechanisms produce very different structures. With n-type doping, the carrier density among the pores is controlled by light intensity, i.e. the zone among the pore can be completely depleted. This means that high aspect ratio are reachable (see Fig. 11), because the lateral growth of the pores is perfectly inhibited. With p-type doped substrates, we can only reduce the lateral growth of pores by choosing the opportune substrate resistivity. In both cases, to obtain a periodic structures, it is required a lithographic step to define the position of the initial etch pits. After the lithographic, a chemical attack, in KOH or TMAH, forms inverted pyramids where the electrochemical attack initiates.

On some photonic crystals formed on n-type doped substrates, the dispersion properties of photons have been measured by variable angle reflectance with an FTIR-spectrometer [32]. By reporting the energy position of the spectral features of the reflectance spectra as a function of the light wave vector it is possible to build the energy-dispersion of the photons in the photonic crystals (Fig. 13). The experimental data are in extremely and surprisingly good agreement with respect to the calculated values, which are simply based on the knowledge of the filling factor and the crystal lattice period.

On photonic crystals developed on p-type doped silicon we observed the possibility to induce a modification of the final structure with respect to the one defined by lithography. In particular, it is possible to exploit the lateral growth of pores to obtain two different effects. The first consists in an almost complete dissolution of the pore walls. In this way it is possible to pass from a structure based on air holes in silicon, to a new one formed by silicon pillars in air (Fig. 14). The second possibility is to induce the growth of pores in interstitial lattice positions. This result could be achieved when the separations between two adjacent pores are larger than the sum of their space charge regions. Photonic crystals formed on p-type doped silicon have a much large degree of tuneability.

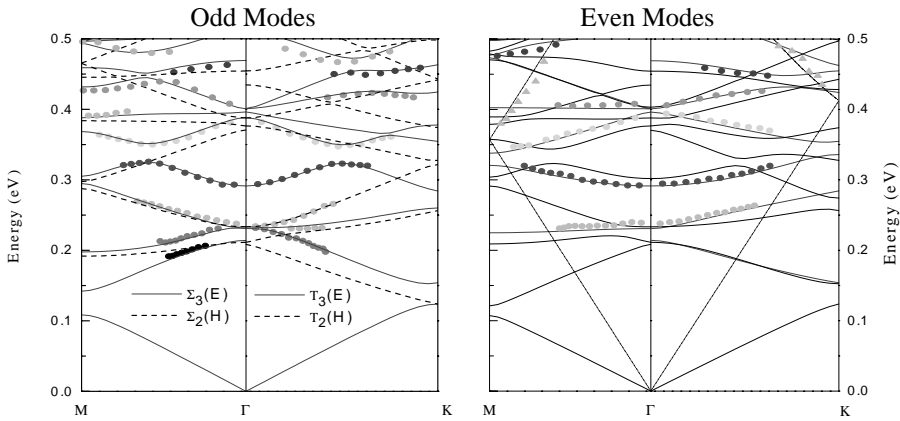


Fig. 13. Critical points in variable angle reflectance of representative photonic crystals. The lines are the theoretical value, the points are the experimental measures. The left panel refers to photonic modes of odd symmetry, while the right panel to photonic modes of even symmetry. The photonic crystals parameters are: triangular lattice of air holes in silicon, lattice parameter $a = 2\ \mu\text{m}$, radius of pores $r = 0.24a$.

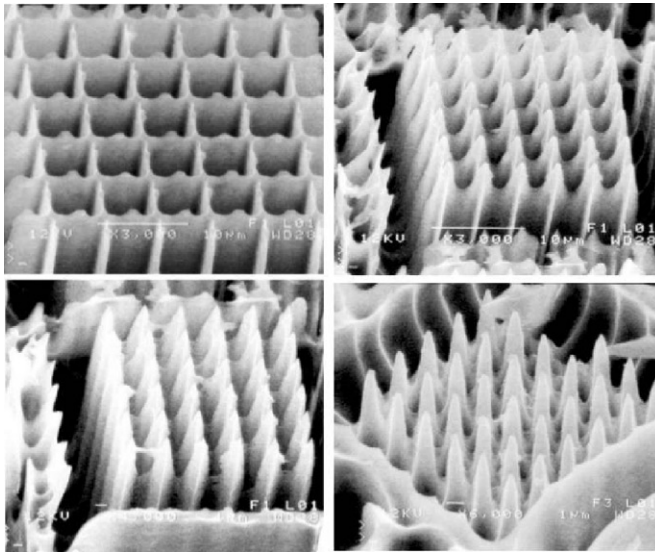


Fig. 14. Change in the kind of photonic crystals in p-type doped silicon as the lattice parameter is reduced. The lattice parameters are from the left up corner: 6, 4, 3 and $2\ \mu\text{m}$.

6. Interferometric method for monitoring electrochemical etching of porous silicon

Porous silicon is the prototype of all low dimensional silicon systems [4]. For its formation, a critical parameter is the knowledge of the etching depth dependence of

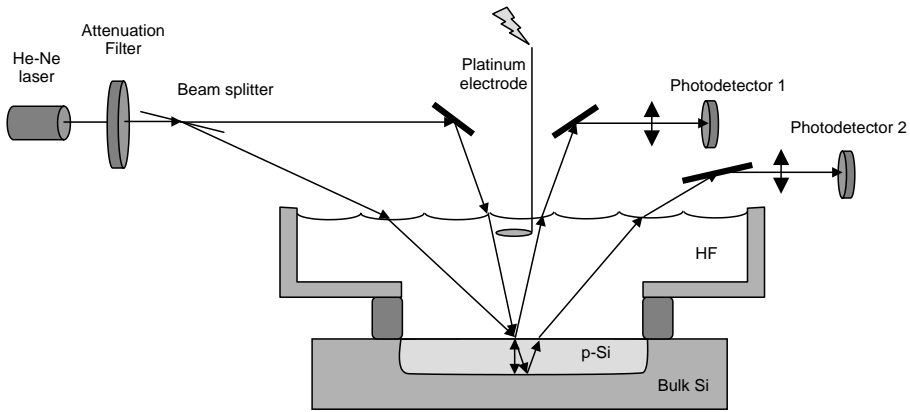


Fig. 15. Experimental set-up used for the two-beam interference method.

the sample properties. To this aim, we have developed an in-situ technique to monitor the index of refraction as well as the etch rate during the electrochemical attack. This is based on the measure of the interference fringes of two beams with different angles of incidence on the sample (Fig. 15). With this technique we have measured the inhomogeneity in the etch process of porous silicon layers, which is an essential issue to make good quality optical microcavities or photonic crystals with this material [4,24].

Assuming no lateral inhomogeneity, we can calculate the optical path traveled by a beam in a round trip inside a thin porous layer with any index of refraction profile $n(z)$. If this beam interferes with the one reflected at the surface, the optical path difference D will be given by:

$$D = 2 \int_0^l \sqrt{n(z)^2 - n_{\text{HF}}^2 \sin^2 \theta} \, dz + \varphi_0 - \varphi_1, \quad (2)$$

where l is the thickness of the porous layer, $n(z)$ the refractive index profile, n_{HF} the refractive index of the electrochemical solution, θ the incident angle of the beam, and φ_0, φ_1 , the phase changes produced in the reflection at the electrochemical solution-porous layer and porous layer-substrate interfaces. During the etch, l is a function of time. We will approximate φ_0 and φ_1 with constants.

The quantity experimentally measured is not D but its change rate dD/dt . Interference will be constructive when D corresponds to an integer multiple of the wavelength λ_0 . In this case, a maximum in reflection will be measured. Thus, the frequency of the reflection signal as a function of time will be:

$$\nu(t) = \frac{1}{\lambda_0} \frac{dD}{dt}(t). \quad (3)$$

To solve this derivative, we assume that the index of refraction does not change with time but only with the depth. This means that we neglect the effect of chemical

etching. Validity of this assumption is supported by the results. Then,

$$v(t) = \frac{1}{\lambda_0} 2 \sqrt{n^2(z) - n_{HF}^2 \sin^2 \theta} \frac{dl}{dt} \tag{4}$$

which is the frequency of the oscillations observed with an incident angle θ . With algebra manipulations and knowing the frequency observed for two different angles θ_1 and θ_2 , we get:

$$n(t) = n_{HF} \sqrt{\frac{v_1^2(t) \sin^2 \theta_2 - v_2^2(t) \sin^2 \theta_1}{v_1^2(t) - v_2^2(t)}}$$

$$\frac{dl}{dt} = \frac{\lambda_0}{2n_{HF}} \sqrt{\frac{v_1^2(t) - v_2^2(t)}{\sin^2 \theta_2 - \sin^2 \theta_1}} \tag{5}$$

Experiments were performed on p⁺-type doped wafers (0.01 Ωcm) with an electrolyte formed by 48% aqueous HF mixed with ethanol in a concentration of 15%. Fig. 16 reports the reflection signals for two angles of observation during an experiment where the etching was performed with a constant current input of 25 mA/cm². The deduced etch rate and porosity as a function of time are plotted in Fig. 17. We have estimated the porosity (volumetric fraction of air in the porous layer) from the refractive index by making use of Bruggeman effective medium approximation [4]. The etch rate has been fitted by a straight-line. An indirect estimation of the porosity gradient is possible by making use of the following equation (deduced from Faraday’s equation):

$$\frac{dl}{dt} \mathcal{P} = \frac{j}{Nev} \tag{6}$$

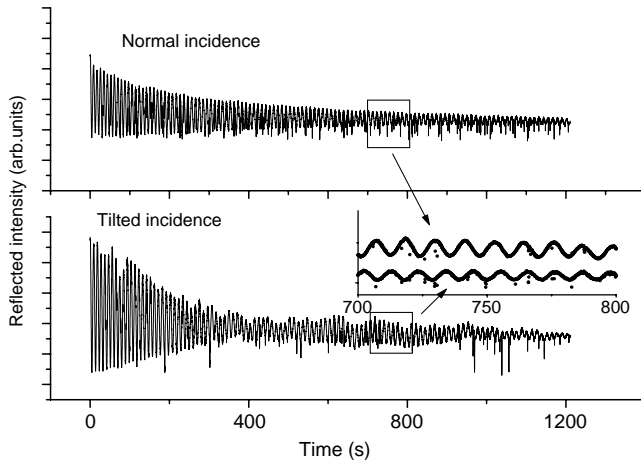


Fig. 16. Plot of each of the two interference patterns observed during the etching process for a constant current density of 25 mA/cm². The frequency difference observed is what will give us the growth parameters.

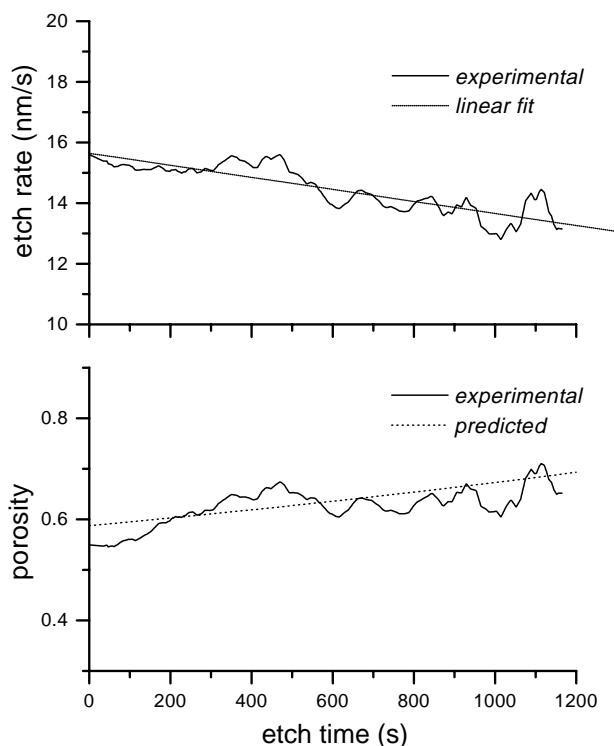


Fig. 17. Etch rate (upper panel) and porosity (lower panel) measured via the two-beam interferometry method for a constant current density of 25 mA/cm^2 . The predicted porosity calculated with Faraday's equation is given by the dotted line.

being \mathcal{P} the porosity, j the current density, N the number of bulk silicon atoms per volume unit, e the electronic charge, and v the valence, which is the number of electrons necessary to dissolve one silicon atom (assumed 3.4 [33]). In Fig. 17, the indirect estimation is compared to the measured \mathcal{P} , a good agreement can be observed. The positive gradient in the porosity as a function of time is also in accordance with previous works [34,35]. The total thickness of the porous layer at the end of the etch has been measured by SEM. The comparison between this thickness and the time integration of the etch rate curve yields an error of less than 4%, backing up the reliability of the proposed interferometric technique.

7. Light diffusion in Fibonacci superlattices, evidence of light localization?

Anderson localization is a general feature related to any waves propagating in strongly disordered structures [36].⁵ Localization is not only related to disordered

⁵This work has been supported by the University of Trento through the program Giovani Ricercatori M.A.R.C. under the responsibility of dott. Luca Dal Negro and in collaboration with the “waves in

electronic systems but it has recently been reported for acoustic [37] as well as for optical waves [38]. In the strong scattering regime, the diffusion constant of any particles (photons, electrons, acoustic waves, etc.) is found to disappear if the scattering mean free path becomes smaller than some critical value. In this regime, the particles become localized. This phenomenon can be described as due to an interference effect between counter propagating waves. Light localization in fully random three dimensional systems has been demonstrated for strongly scattering semiconductor powders [39]. When the scattering mean free path becomes comparable with the wavelength of light, a freely propagating wave can no longer build up over one oscillation of the electric field and the light becomes localized. Very recently it has been theoretically demonstrated that localization occurs not only in disordered systems but also in deterministic quasi-periodic ones [40], such as one dimensional Fibonacci quasi-crystals. Quasi-crystals are perfectly ordered structures, where the Bloch theorem is not applicable since there is no translational symmetry. Furthermore, in such a systems the wavefunctions are not exponentially localized as in the purely disordered systems. It can be said that quasi-crystals represent to a certain extent an intermediate case between periodic and disordered systems.

We have grown porous silicon Fibonacci multilayers by stacking different layers according to the simple Fibonacci generation sequence $F_n = F_{n-2} + F_{n-1}$. It is interpreted here as a substitutional rule $S_n = S_{n-2}S_{n-1}$, where $S_0 = A$, $S_1 = B$, being A and B the two generating porous silicon layers. For layer A we used a thickness of 190 nm and a porosity of 69%, while for layer B a thickness of 85 nm and a porosity of 48%. Following the generation rule, we can obtain any sequences: $S_0 = A$, $S_1 = B$, $S_2 = AB$, $S_3 = BAB$, $S_4 = ABBAB$, $S_5 = BABABBAB$ and so on for the higher order elements. Due to the high control we achieve in the porous silicon growth, we have grown Fibonacci elements up to order 12 (233 layers) and 13 (377 layers).

Fig. 18 shows a typical transmission spectrum for a high order Fibonacci structure together with a transfer matrix simulation. Increasing the number of the Fibonacci elements, many sharp peaks appear in the transmission spectrum, and in the limit of a Fibonacci of infinite order all of these peaks represent localized states and the transmission spectrum becomes of a fractal shape. Up to now there are no experimental evidence of such localized states for finite size Fibonacci quasicrystals, where localized and extended states could mix and coexist. In Fig. 18 in the region around 5000 cm^{-1} a “pseudo band-gap” develops in the structure, due to the presence of a superimposed short-range periodicity.

We have investigated the time dynamics of ultrashort (femtosecond) laser pulses transmitted through a Fibonacci structures of order 12 (233 layers) to study the nature of the photon states. To the best of our knowledge this is the thicker Fibonacci structure that has been fabricated up to now. We have used a time resolved phase sensitive interferometric technique [41,42]. As laser source we have

(footnote continued)

complex media” group of Prof. Ad. Lagendijk at the Van der Waals—Zeeman Institute of Amsterdam and with Dr. D. Wiersma at the L.E.N.S. in Florence.

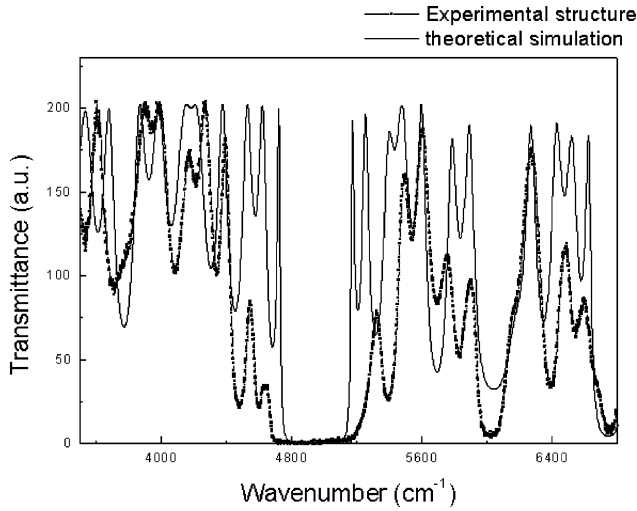


Fig. 18. Experimental transmission spectra of a Fibonacci 11 structure with 144 layers (dotted-line graph) and simulated transmission (line graph) for normal incidence. The measurement has been performed by a standard Biorad Fourier infrared spectrometer. The fine narrow peaks (probably localized states) of the simulated structures are hardly recovered in the experimental spectrum due to the large angular spreading of the spectrometer source.

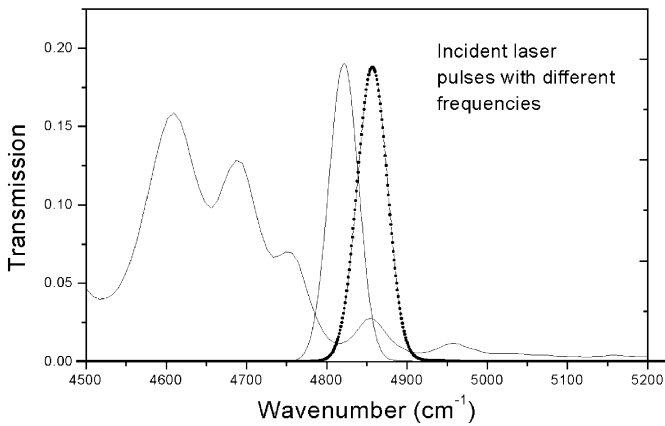


Fig. 19. Pseudo band-edge of a Fibonacci (order 12–233 layers) quasi-crystal. The gaussian profiles are the envelopes of two laser pulses used in the experiment to probe the propagation dynamics of light inside the structure.

used a femtosecond Ti:Sa laser with an OPAL tunable parametric oscillator for wavelength tuning.

By using different laser frequencies we have spanned the band-edge of the sample at 5000 cm^{-1} (Fig. 19). In Fig. 19 we also show two incident laser pulses with

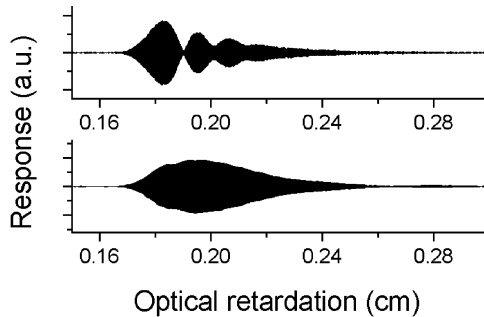


Fig. 20. Optical response functions of the 12-order Fibonacci quasi-crystal corresponding to two different laser frequencies resonantly with the pseudo band-edge.

different frequencies in the band-edge. When passing through the structure, the incident laser pulses are strongly distorted and delayed (Fig. 20). To our knowledge no such a dramatic effect on the pulse dynamics has been previously reported. When the incident laser pulse enters the band-edge of the Fibonacci it is strongly delayed because of the reduced “group velocity” (energy velocity) at the band-edge, and if the incident pulse can excite more than one pseudo-localized narrow states at the band-edge, the pulse distortion is modulated by the coherent beatings of such states. The beating frequency is indeed equal to the frequency separation of these two states. Furthermore, different pseudo-band-edge states can be excited by the incoming pulse envelope originating different coherent beatings. Fig. 20 shows a modulated response function and a delayed transmitted pulse corresponding to the incident pulses reported in Fig. 19. Only one of these two incident pulses is able to excite two narrow modes at the band-edge, and its time response becomes strongly modulated (upper panel). When the incident pulses are far away from the band-edges, no such effects have been measured. We believe that the nature of the band-edge states originating such strong beatings is that of “pseudo-localized” states, as predicted by theory for very thick structures.

8. Porous silicon as the sensing material for optoelectronic gas sensors

The optical properties of porous silicon microcavities are strongly dependent on the environment [4,43].⁶ For highly luminescent samples both the luminescence intensity and the peak position are affected by organic substances, giving the possibility to obtain a dual-parameter optical sensors. While the peak position depends on the organic compound refractive index, luminescence intensity depends

⁶This work has been made in collaboration with Prof. Sberveglieri and co-workers of University of Brescia and financed by INFM through the project SMOG and by PAT through a project coordinated by Prof. G. Soncini.

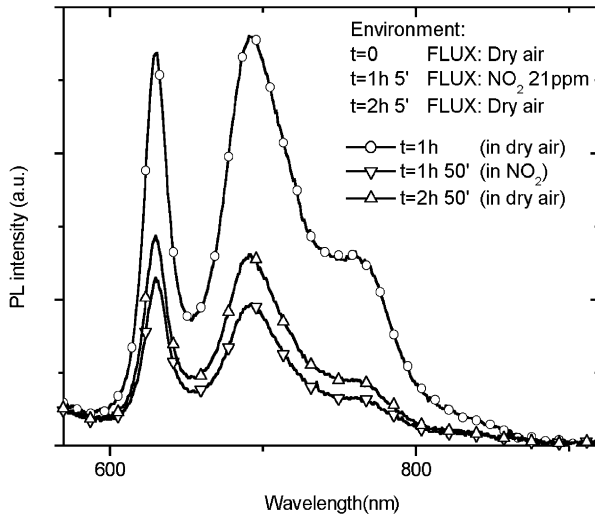


Fig. 21. PL spectra of a high resistivity PSM, under controlled flux (0.31/m), of dry air (circles), dry air + NO₂ (21 ppm, downward triangles), and back to dry air (upward triangles). Timing of switching of flux, as well as of spectra acquisition, is indicated in the plot (room temperature).

mainly on its low frequency dielectric constant [43]. This allows discriminating between different substances and makes possible to fabricate a multiparametric gas sensor which senses both optical properties (microcavity peak position and luminescence intensity) and electrical properties (conductance).

Here we report on experiments which demonstrated the selectivity of the sensors and posed upper limits to their sensitivity. The sensor is based on porous silicon microcavities which have been obtained in a way similar to the one described in Ref. [44]. We aimed to demonstrate the effectiveness of the sensor as detector of NO₂, an hazardous air pollutant. In Fig. 21, it is shown the luminescence spectrum for different concentrations of NO₂. We can see a significant quenching of the luminescence. However no shift in the spectral features are observed. This contrasts to most of the behaviors that this kind of sensor has when exposed to other gases [43]. In Fig. 22 we show the response of our microcavity to the presence of ethanol: no quenching of the luminescence is observed while a clear spectral shift of the luminescence features is measured. In this way a good selectivity of the sensor to NO₂ can be inferred. As far as the sensitivity, conductance measurements are reported in Fig. 23. Clearly, the presence of NO₂ can be detected down to a concentration of 1 ppm. Also the current recovers completely to the initial value after dry air is restored. The relative response $\Delta G/G$ of the PSM was of 6.6 at 2 ppm. Thus the presence of NO₂, in concentrations of the order of few to few tens of ppm, causes (a) PL quenching (b) conduction enhancement (c) no cavity peak-shift. All this measurements demonstrate the feasibility of a multiparametric gas sensor able to distinguish and to measure different gas components. In the special case of NO₂, as it

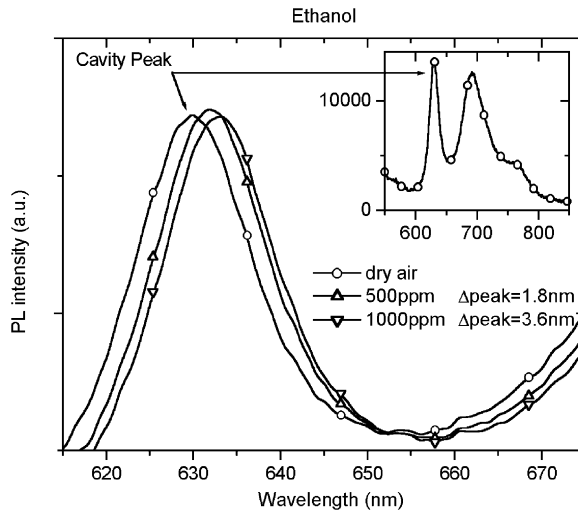


Fig. 22. PL spectra of a high resistivity PSM, under controlled flux of air containing ethanol with the indicated concentration. Dry air (circles), dry air+ethanol (500 ppm: upward triangles, 1000 ppm: downward triangles). The inset show the overall spectrum.

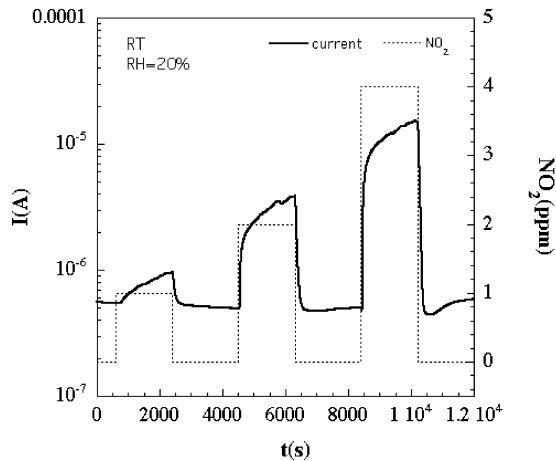


Fig. 23. Electrical current through a low resistivity PSM under controlled flux (0.31/m) of humid air (20%) containing 1, 2 or 4 ppm of NO_2 .

is an air pollutant, its concentration sensing is a very valuable issue due to its wide range of applications.

9. Conclusions

In this paper we have shown some of the interesting properties which arise when silicon is tighten into nanoscale objects: light amplification due to the emergence of

radiative interface states, non-linear optical properties due to the quantum confinement enhanced third order susceptibility, sharp room temperature luminescence due to the spatial redistribution of spontaneous emission in an optical microcavity activated by silicon superlattices, selective sensing of poisonous gas due to the enormous internal surface of porous silicon. Other novel properties crop up when silicon is structured in such a way that the propagation of light through it is modified: beating of disordered slow down photon modes in Fibonacci one-dimensional crystals, modified energy dispersion of photons in two-dimensional macroporous silicon. All these novel properties can be engineered to open new perspectives in photonic applications of silicon.

Acknowledgements

The work here reported is the outcomes of numerous collaborations we have. We thank all the partners of the various institutions who have contributed to these results and the various sponsor agencies who have financed our work.

References

- [1] Ball P. *Nature* 2001;409:974.
- [2] Pavesi L, Dal Negro L, Mazzoleni C, Franzò G, Priolo F. *Nature* 2000;408:440.
- [3] Silicon based microphotonics: from basics to applications, Proceedings of the E. Fermi Schools: Course CXLI, Bisi O, Campisano SU, Pavesi L, Priolo F, editors. Amsterdam: IOS press, 1999.
- [4] Bisi O, Ossicini S, Pavesi L. Porous silicon: a quantum sponge structure for silicon based optoelectronic. *Surf Sci Rep* 2000;264:1–126.
- [5] Wolkin MV, Jorne J, Fauchet PM, Allan G, Delerue C. *Phys Rev Lett* 1999;82:197–200.
- [6] Shaklee KL, Nahaory RE, Leheny RF. *J Lumin* 1973;7:284–309.
- [7] Yariv A. *Quantum electronics*, 2nd edition.. New York: John Wiley & Sons, Inc., 1975.
- [8] Blood P. *IEEE J Quantum Electron* 2000;36:354–62.
- [9] Kirstaedter N, et al. *Appl Phys Lett* 1996;69:1226–8.
- [10] Lingk C, von Plessen G, Feldmann J, Stock K, Arzberger M, Bohm G, Amann MC, Abstreiter G. *Appl Phys Lett* 2000;76:3507–9.
- [11] Henari FZ, Morgenstern K, Blau WJ, Karavanski VA, Dneprovskii VS. *Appl Phys Lett* 1995;67:323 and references therein.
- [12] Mansoor Sheik-Bahae, Alli a Said, Tai-Huei Wei, David J Hagan, Van Stryland EW. *IEEE. J Quantum Electronics* 1990;QE26:760.
- [13] Iacona F, Franzo G, Spinella C. *J Appl Phys* 2000;87:1295 and references therein.
- [14] Reitze DH, Zang tR, Wood WmM, Downer MC. *J Opt Soc Am B* 1990;7:84.
- [15] Vijaya Prakash G, Daldosso N, Elena Degoli, Iacona F, Pucker G, Cazzanelli M, Rocca F, Gaburro Z, Dalba P, Ceretta Moreira E, Pacifici D, Franzò G, Priolo F, Arcangeli C, Filonov AB, Stefano Ossicini, Pavesi L. *J Nano Sci Nano Tech* 2001;1:159.
- [16] Reintjes JF, McGroddy JC. *Phys Rev Lett* 1973;30:901.
- [17] Vogel EM, Weber MJ, Krol DM. *Phys Chem Glass* 1991;32:231.
- [18] Chen R, Lin DL, Mendoza B. *Phys Rev B* 1993;48:11879.
- [19] Vijaya Lakshmi S, Shen F, Grebel H. *Appl Phys Lett* 1997;71:3332.
- [20] Vijaya Lakshmi S, George MA, Grebel H. *Appl Phys Lett* 1997;70:708.
- [21] Pucker G, Cazzanelli M, Bellutti P, Gatterer K, Spinella C, Pavesi L. *J Appl Phys* 2000;88:6044.

- [22] Mulloni V, Chierchia R, Mazzoleni C, Pucker G, Pavesi L. *Phil Mag B* 2000;80:705.
- [23] Confined electrons and photons, Weisbuch C, Burstein E, editors. Boston: Plenum Press, 1995.
- [24] Pavesi L. *La Rivista del Nuovo Cimento* 1997;20:1.
- [25] Pavesi L, Panzarini G, Andreani LC. *Phys Rev B* 1998;58:15794.
- [26] Ossicini S, Degoli E. In: Pavesi L, Buzaneva E, editors. *Frontiers of Nano-Optoelectronic Systems*. Dordrecht: Kluwer Academic Publishers, 2000. p. 147–60.
- [27] Jannopoulos JD, Meade RD, Winn JN. *Photonic crystals: molding the flow of light*. Princeton, NJ: Princeton University Press, 1995.
- [28] Lehmann V, Gösele U. *Appl Phys Lett* 1991;58:856.
- [29] Föll H, Cartensen J, Christophersen M, Hasse G. *Phys Stat Sol A* 2000;182:7.
- [30] Lehmann V, Föll H. *J Electrochem Soc* 1990;137:653.
- [31] Lehmann V, Rönnebeck S. *J Electrochem Soc* 1999;146:2968.
- [32] Galli M, et al. *Phys Rev Lett*, submitted.
- [33] Gaburro Z, You H, Babic D. *J Appl Phys* 1998;84:6345.
- [34] Thönissen M, Billat S, Krüger M, et al. *J Appl Phys* 1996;80:2990.
- [35] Thönissen M, Berger MG, Billat S, et al. *Thin Solid Films* 1997;297:92.
- [36] Anderson PW. *Phys Rev* 1958;109:1492.
- [37] Sorek Y, Reisfeld R, Weiss AM. *Chem Phys Lett* 1995;244:371.
- [38] van Albada MP, Lagendijk A. *Phys Rev Lett* 1985;55:2692.
- [39] Wiersma DS, Bartolini P, Lagendijk A, Righini R. *Nature* 1997;390:671.
- [40] Machida K, Fujita M. *Phys Rev B* 1986;34:7367.
- [41] Rik HJ Kop, Sprik R. *Rev Sci Instrum* 1995;66:5459.
- [42] Arnout Imhof, Willem L Vos, Sprik R, Lagendijk A. *Phys Rev Lett* 1999;83:2942.
- [43] Mulloni V, Pavesi L. *Appl Phys Lett* 2000;76:2523.
- [44] Gaburro Z, Daldosso N, Pavesi L, Faglia G, Baratto C, Sberveglieri G. *Appl Phys Lett* 2001; 78:3744.